Supplementary Information

Double bilayer to study nonequilibrium environmental response of GIRK2 in complex states

*Corresponding author:

Chenyi Liao (cliao2@dicp.ac.cn); Guohui Li (ghli@dicp.ac.cn)

Table S1. A summary of simulations.

	No. of atoms	Box size (nm^3)	MD Simulation (ns)	Umbrella sampling (ns)
Single bilayer systems				
random PIP2	220186	123×123×157	1374, 1017, 1089, 1017	100, 100, 100
PIP2-bound GIRK2	220478	123×123×157	1007, 1096, 1031, 1071	100, 100, 100
Gβγ-bound GIRK2	544377	180×180×178	1120, 1190, 1180, 1440	100, 100, 100
Double bilayer systems				
PIP2-bound GIRK2	440952	115×115×325	2606, 1185, 2051	100, 100, 100
Gβγ-bound GIRK2 for inward K^+	1088754	170×170×370	1876, 1986, 3358	100, 100, 100
Gβγ-bound GIRK2 for outward K^+	1088754	170×170×370	1425, 1455	
Gβγ-bound GIRK2 for inward K^+ and Na^+	1088754	170×170×370	1110, 1324	

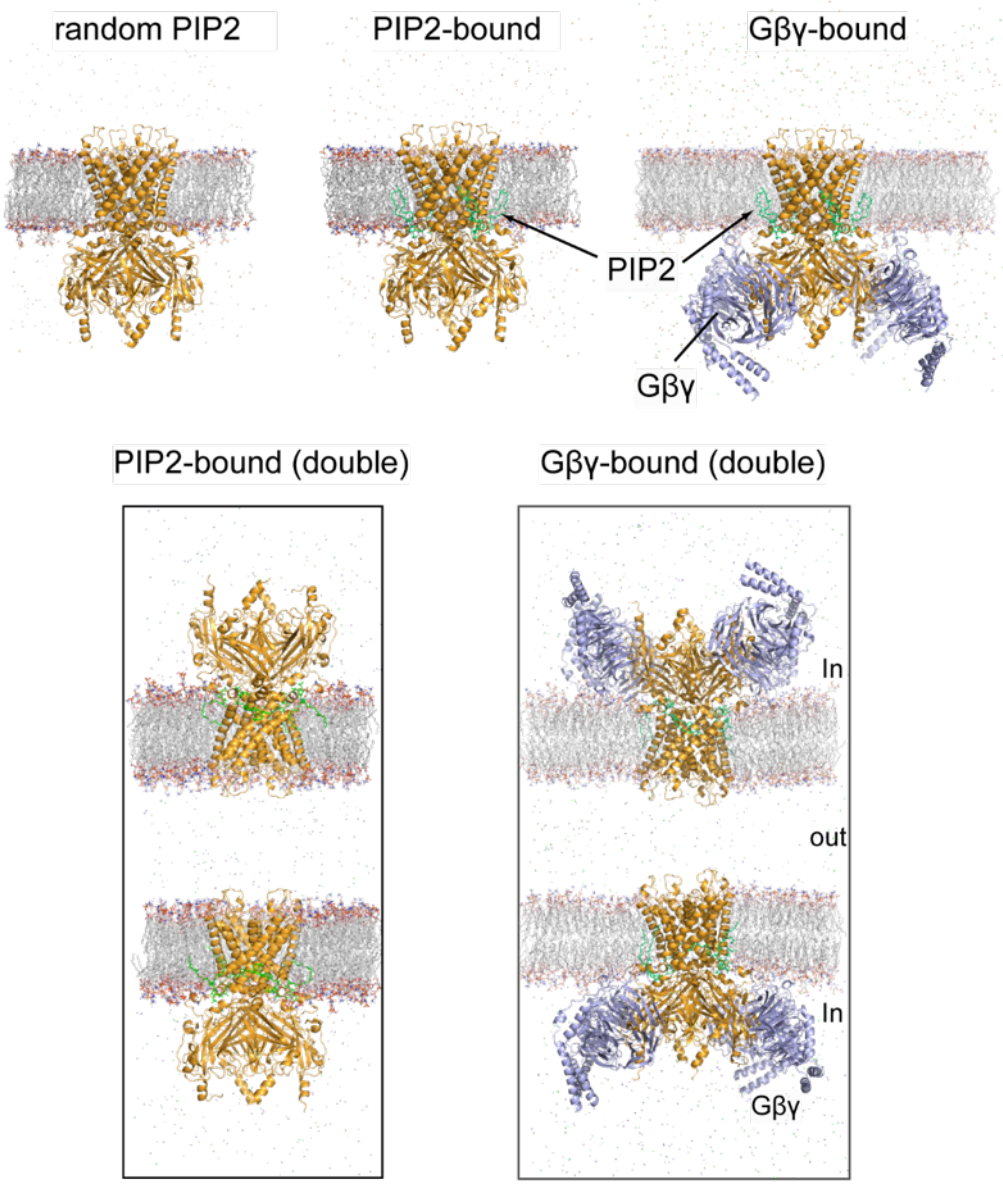

Fig. S1 Five systems in current study: random PIP_2, PIP_2-bound, and Gβγ-bound states in single bilayer; PIP_2-bound and Gβγ-bound states in double bilayer. GIRK2 is shown in orange cartoon; Gβγ is shown in light blue cartoon; bound-PIP_2 is shown in green stick.

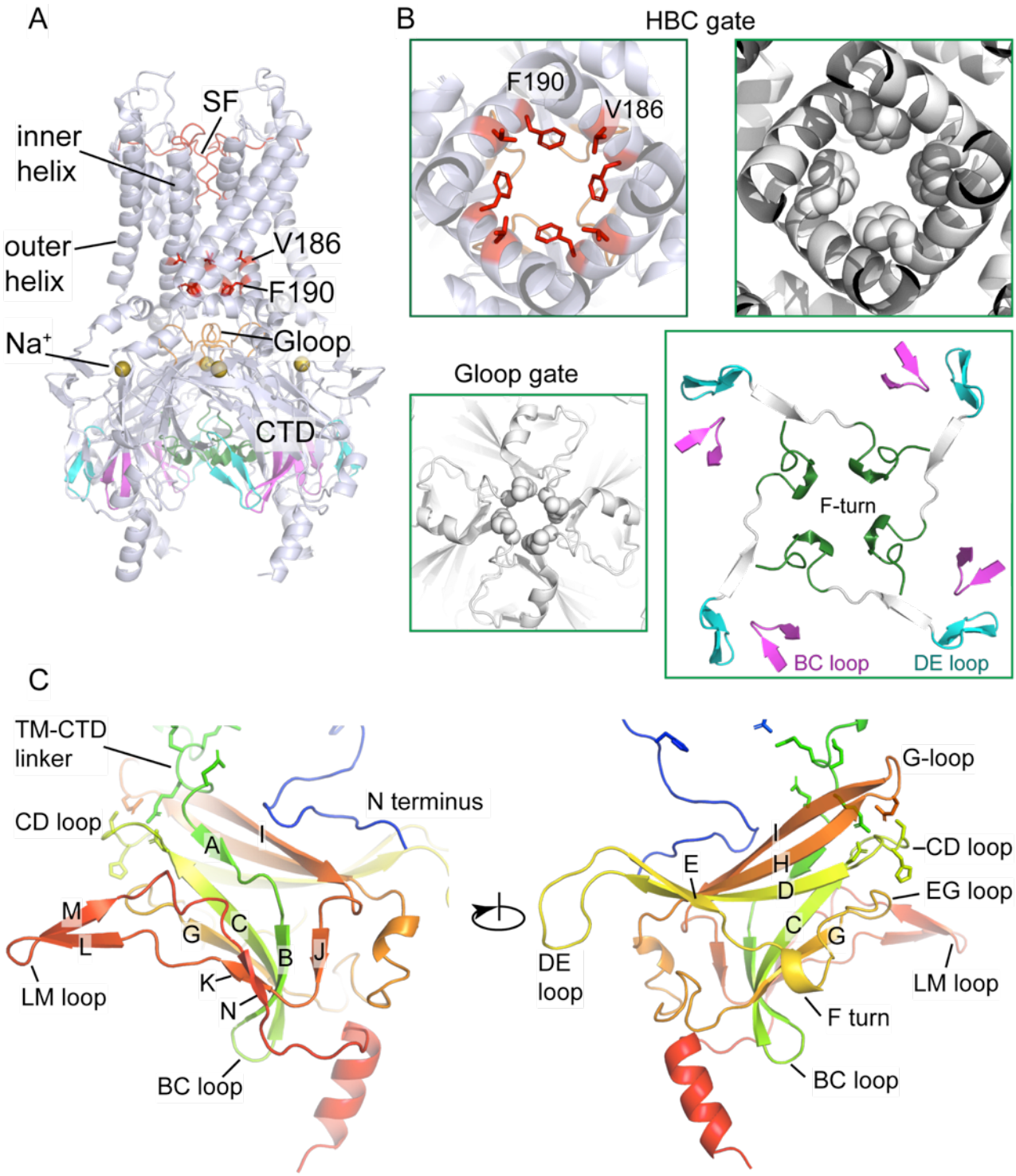

Fig. S2 GIRK2 structure. (A) Side view of GIRK2 with the inner and outer helix consisting the transmembrane helices (TMs) domain; (B) top-down views of the HBC gate comprising V186 and F190, the G-loop gate (M311-M317), DE loop (in res. 245-253), BC loop (in res. 212-219), and F-turn (in res. 262-272) in CTD; (C) side views of CTD in one GIRK2 subunit with β-strands and loops labeled.

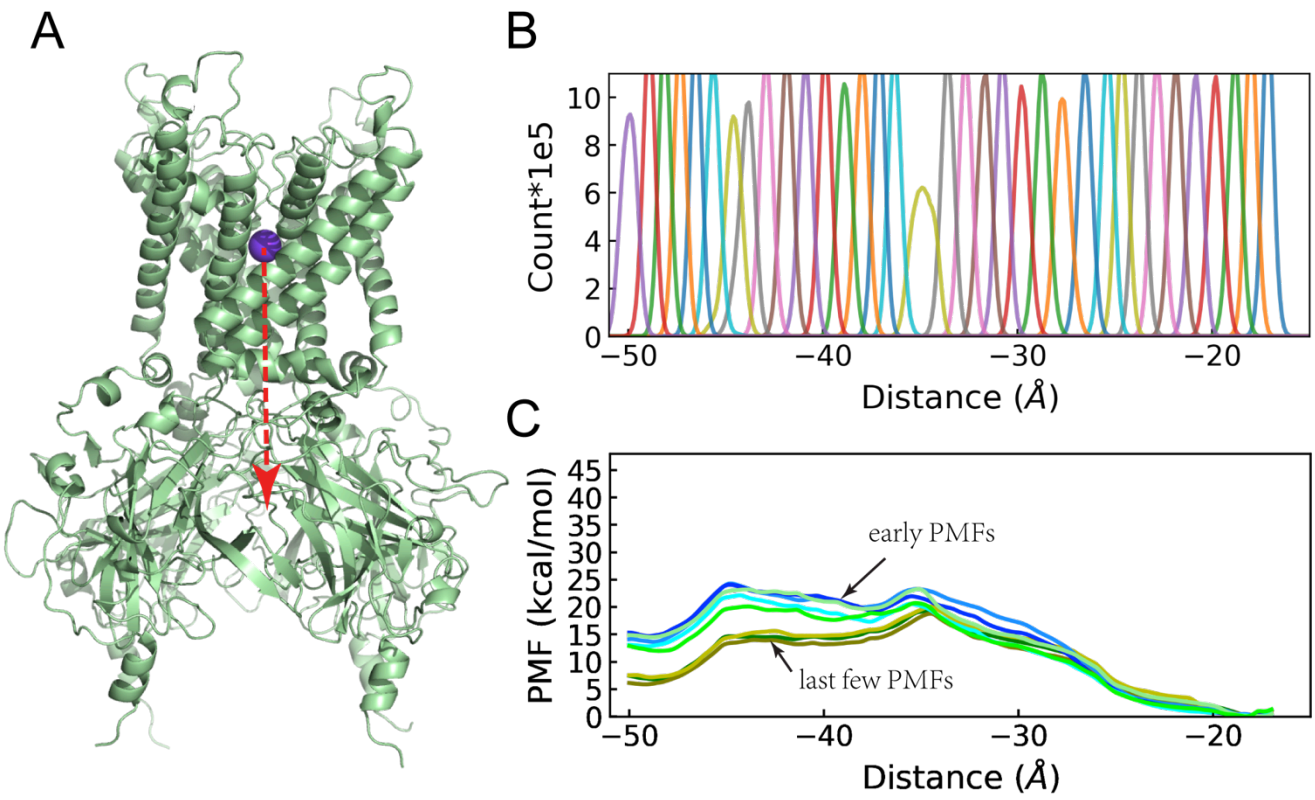

Fig. S3 Umbrella sampling scheme for K^+ PMF calculation. (A) Demonstration of a K^+ pulled along the GIRK2 channel to generate trajectory for initial umbrella sampling windows. (B) Histogram of z-position distributions of K^+ along the channel from 34 windows to show the overlap between adjacent windows. (C) Illustration of PMFs in 10-ns interval in 100 ns constrained MD simulation to check if the PMF calculation was converged. The last three lines in dark green or olive indicated the convergence.

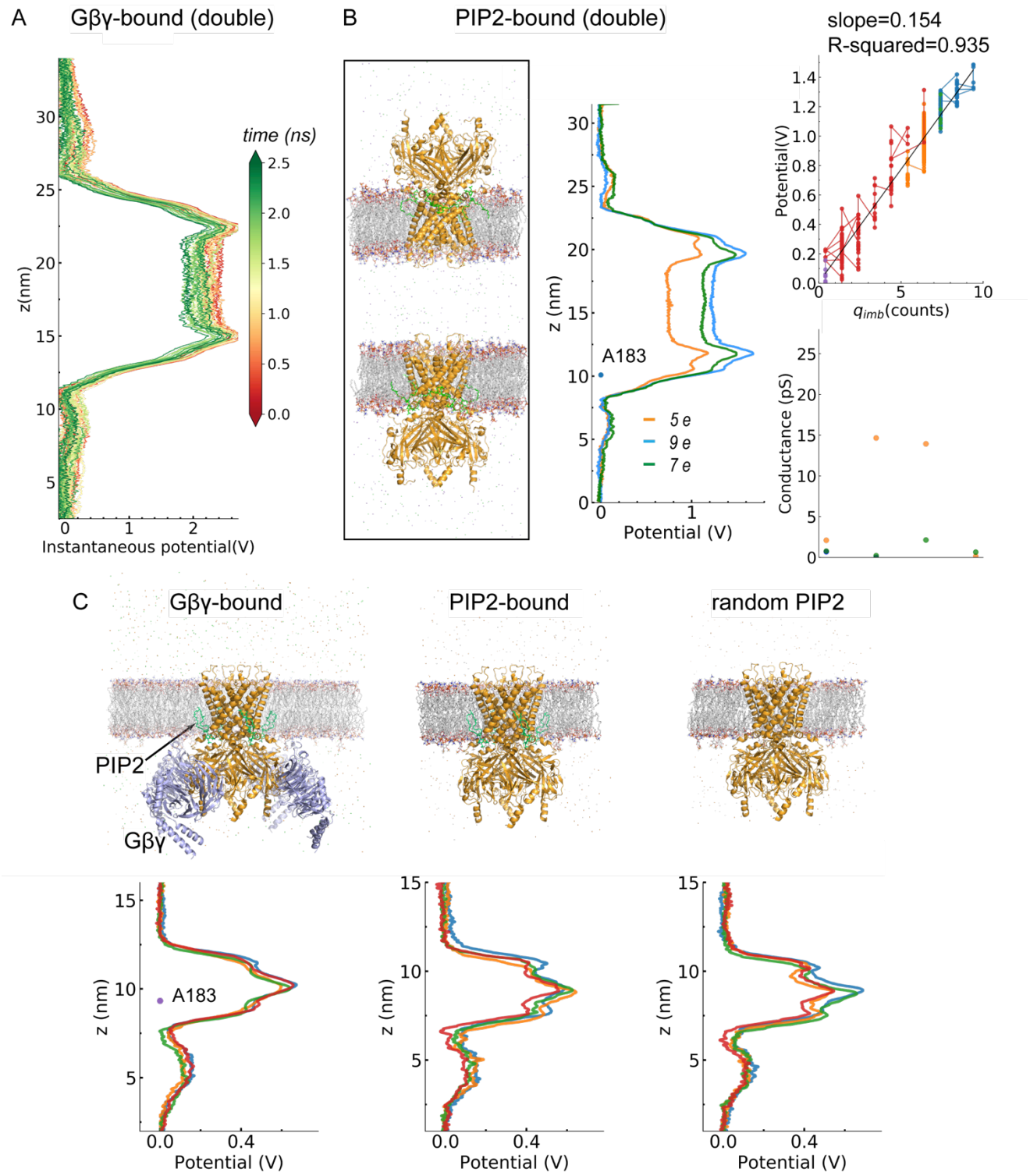

Fig. S4 Electric potentials. (A) Instantaneous electric potentials in the initial 2.48 ns comprising 31 frames (indicated by color bar) in Gβγ-bound double bilayer system. (B) PIP_2-bound double bilayer system and final electric potentials along the z-axis from three independent simulations; relationship between membrane potential and charge imbalance as U=0.154×q_{imb}; ion conductance values corresponding to each discharge process in Fig 2D. (C) Single bilayer systems of Gβγ-bound, PIP_2-bound, and random PIP_2 systems and final

electric potentials along the z-axis from four independent simulations. A183 was labeled as a position marker.

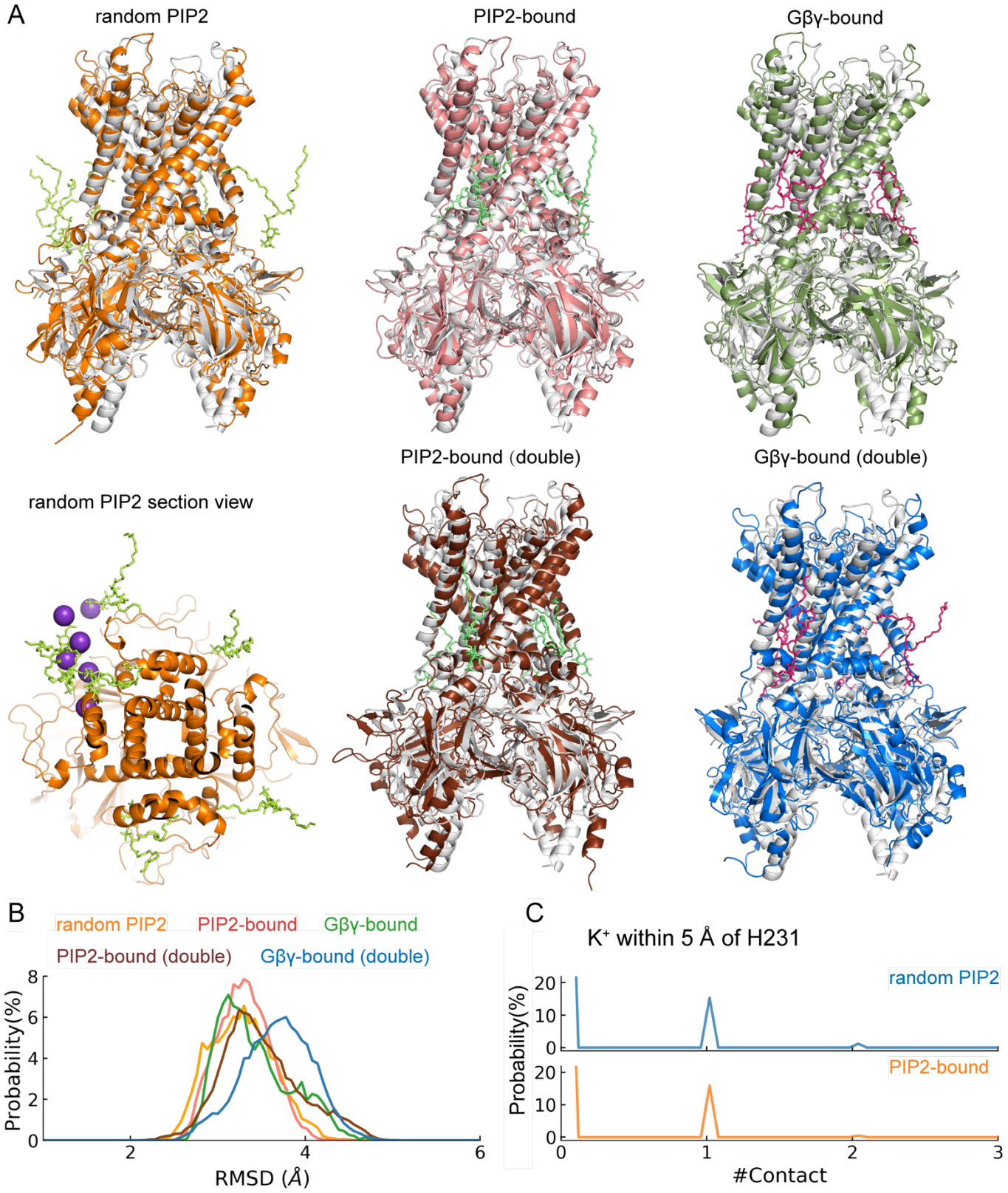

Fig. S5 Structural alignments and interactions with PIP_2 and cations. (A) Structural alignments on crystal structure (PDBID: 4KFM) for representatives of GIRK2 in random PIP_2, PIP_2-bound, Gβγ-bound

single bilayer systems, PIP_2-bound and Gβγ-bound double bilayer systems. PIP_2 molecules are shown in light green or pink sticks. In random PIP_2 system, eventually 4~7 PIP_2 molecules were found gathering around GIRK2 and formed hydrogen bonds particularly with R58 and K62 of GIRK2. A section view of random PIP_2 system is shown with bound PIP_2 molecules and K^+-bridged PIP_2 clusters shown in sticks. K^+ within 4 Å of PIP_2 are shown in purple sphere. (B) Cα RMSD distribution histograms of GIRK2 in random PIP_2, PIP_2-bound, Gβγ-bound single bilayer systems, PIP_2-bound and Gβγ-bound double bilayer systems for inward rectification of K^+. First frame was used as the reference. (C) Distribution histograms of number of K^+ within 5 Å of H231 in random PIP_2 and PIP_2-bound systems without Na^+ ingredient.

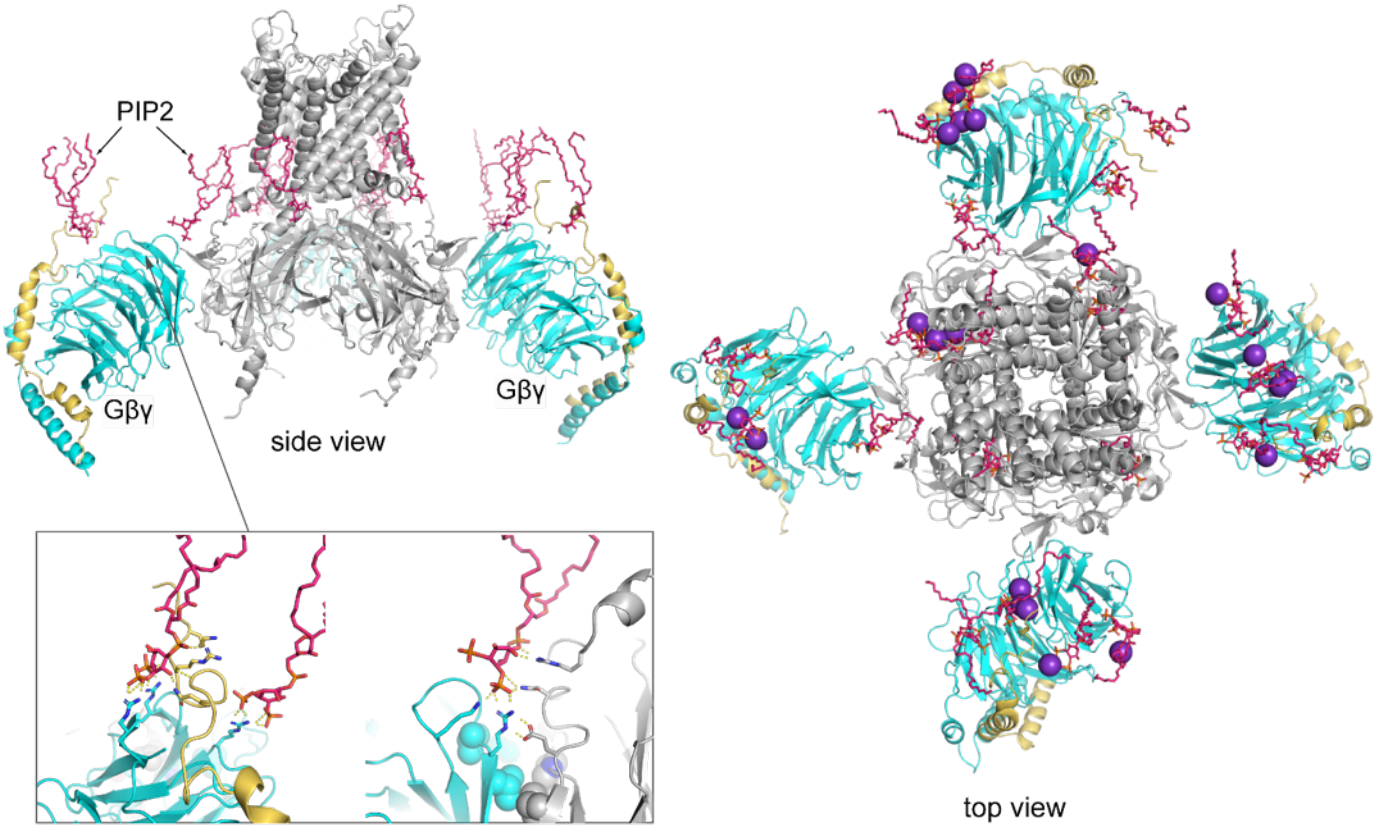

Fig. S6 A final snapshot of Gβγ-bound GIRK2, where PIP_2 molecules (in pink) aggregate and interact with GIRK2 (in gray) and Gβγ (in cyan and yellow). K^+ within 4 Å of PIP_2 are shown in purple sphere in top view. PIP_2 molecule and K^+-bridged PIP_2 clusters not only interact with GIRK2 but also formed strong interactions with Gβγ.

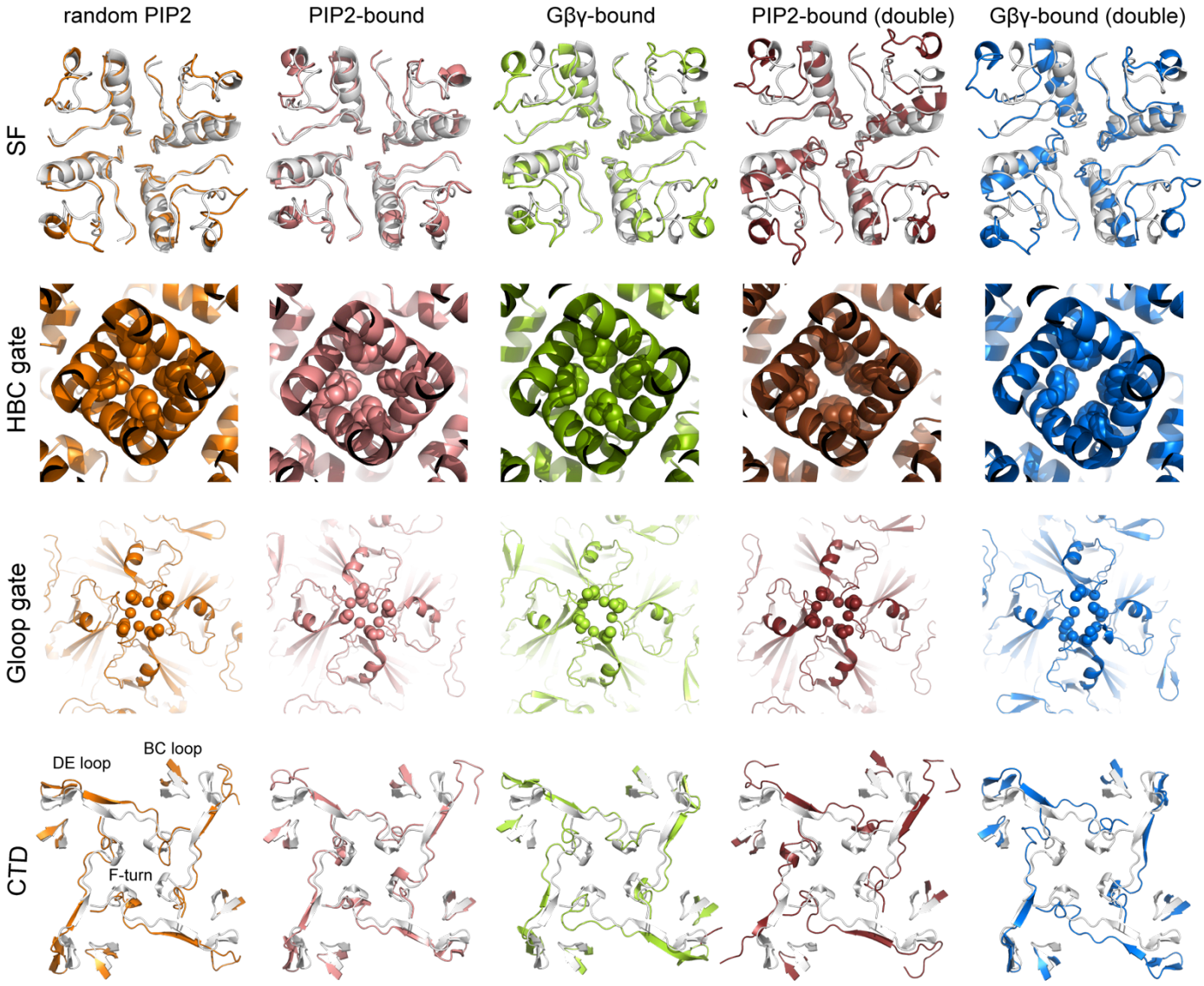

Fig. S7 Top-down views of different sections of representative GIRK2 structures (after structural clustering) in random PIP_2, PIP_2-bound, Gβγ-bound single bilayer systems, PIP_2-bound and Gβγ-bound double bilayer systems after alignments on the crystal structure (PDBID: 4KFM): the selectivity filter (SF), HBC gate with F190 shown in sphere, G-loop gate with G316 and M317 shown in sphere, and the DE loop (in res. 245-253), BC loop (in res. 212-219), and F-turn (in res. 262-272) in CTD.

The HBC and G-loop distances in nonequilibrium condition

The HBC and G-loop Cα distances and minimum distance are commonly used to indicate the opening of GIRKs. However, the distances range exhibited flexible and varied in previous GIRK2 studies [1-3]. In our multiple microsecond MD simulations of single bilayer systems, the F190 Cα distances of HBC were roughly 11~15 Å in random PIP_2, while there was 1~2 Å increasement in PIP_2-bound and Gβγ-bound (Fig S8). The minimum distances of HBC, M311-M317 Cα distances of G-loop, and minimum distances of

G-loop were largely overlapped at 4~6 Å, 14~18 Å, and 5~8 Å respectively in random PIP_2, PIP_2-bound and Gβγ-bound. In response to membrane potential, the HBC and G-loop distances range in PIP_2-bound and Gβγ-bound double bilayer system were generally extended by 2 Å. The distributions of TM2 tilt angle and TM2-CTD dihedral angles were largely overlapped in all systems (Fig S9) comparing with the differentiable distributions in a GIRK2 simulation study [2].

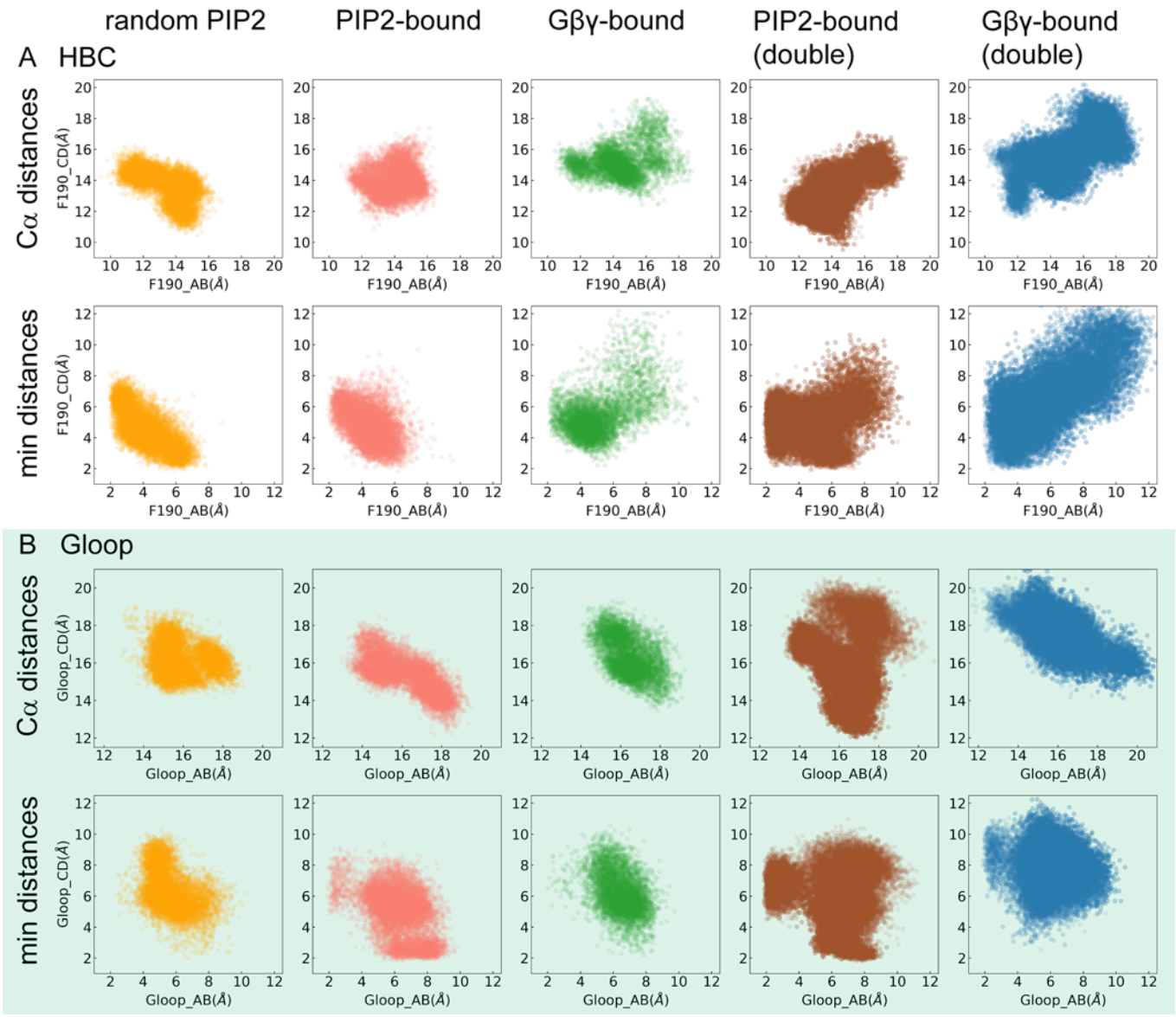

Fig. S8 GIRK2 HBC and G-loop minimum or Cα pair distance distributions in random PIP_2, PIP_2-bound, Gβγ-bound single bilayer systems, PIP_2-bound and Gβγ-bound double bilayer systems. The general stable range of HBC Cα distance were around 11~15 Å in random PIP_2, 11~16 Å in PIP_2-bound and Gβγ-bound system. The general stable range of HBC minimum distance were around 4~6 Å in random PIP_2, PIP_2-bound and Gβγ-bound single bilayer systems. The general stable range of G-loop Cα distance were in 14~18 Å. The general stable range G-loop minimum distance were in 5~8 Å.

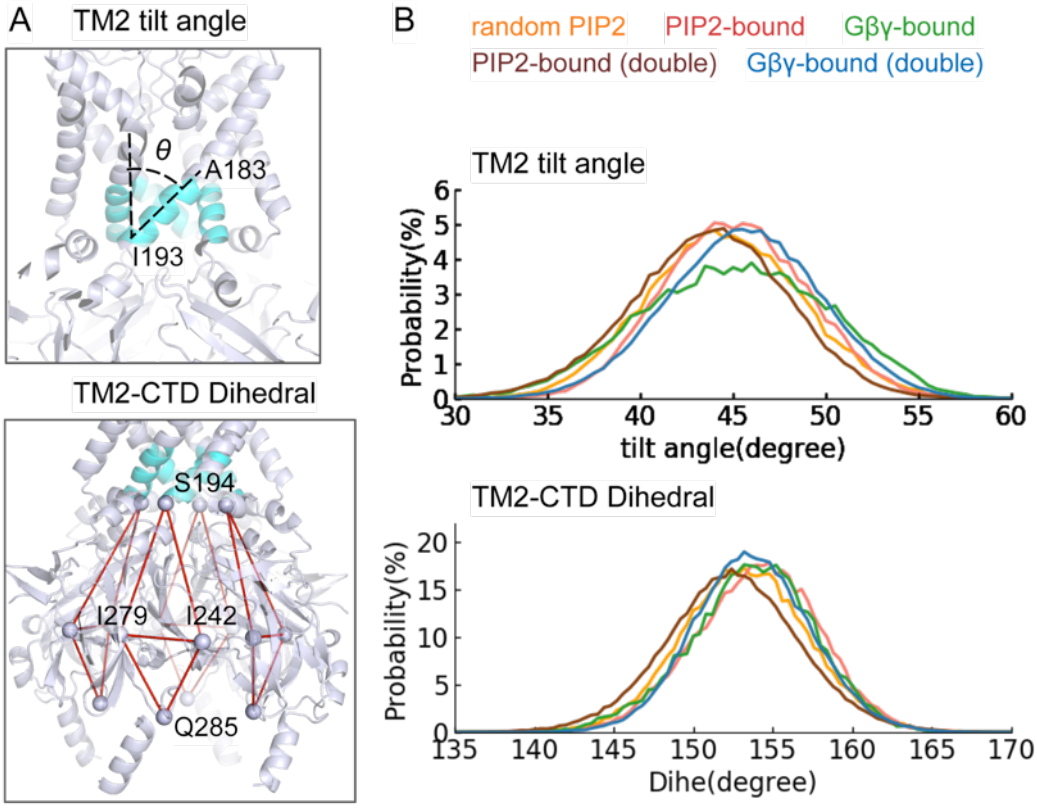

Fig. S9 TM2 tilt angle and TM2-CTD dihedral angles of GIRK2. (A) The TM2 tilt angle defined as the angle between the collection of N-HN vectors and z axis in res. 183-193; the TM2-CTD dihedral angle defined as dihedrals in the alpha carbons of res. S194-I242-I279-Q285. (B) TM2 tilt angle distribution histograms. They are largely overlapped in range of 38~52 degree. (C) TM2-CTD dihedral angle distribution histograms. They are largely overlapped in range of 146~158 degree.

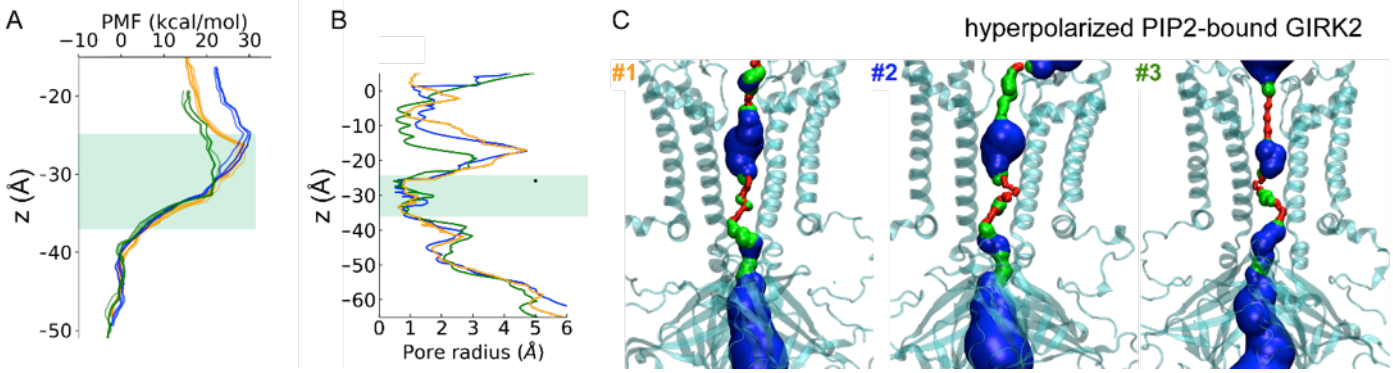

Fig. S10 Free energy landscapes and pore radius along GIRK2 channel in PIP_2-bound double bilayer. US#1 and #2 were under membrane potential of -1.2 V, US #3 was under membrane potential of -0.68 V. (A) PMFs of a K^+ along the channel starting beneath the SF. Each system displayed with three groups (in orange, blue, and green) of PMFs and solvent-accessible pore radius along the channel in (B) 2D graph and (C)3D surface representations. The HBC gate is indicated in light green stripe background in (A) and (B).

Maximum conductance estimation from umbrella sampling

According to the PMF calculations, the rate-limiting region consists of the HBC and G-loop gate (~25 Å). Observed from trajectories, only one cation (K^+ or Na^+) occupy this region at a time. Thus, the rate-limiting region meet the single-ion conductance. In case of low conductance and slow ion motion through the channel, a diffusion model [4] had been used to calculate the crossing rate of ions in terms of one dimensional (1D) position-dependent diffusion coefficient $D(z)$ and a 1D free energy surface $W(z)$. The ion flux (J) through a unit area of the channel can be determined from the 1D Nernst-Planck equation [4-6]

$$J = -D(z)\left(\frac{\mathrm{d}P(z)}{\mathrm{d}z} - \frac{P(z)}{k_{\mathrm{B}}T}\frac{\mathrm{d}W(z)}{\mathrm{d}z}\right), \qquad (1)$$

where k_{B} is Boltzmann's constant and T is the absolute temperature. Both the diffusion coefficient $D(z)$ and energy term $W(z)$ are functions of the ion position along the z axis. $P(z)$ is the ion probability density. At lower voltages (comparable to the cell membrane potential), the maximum single-ion conductance g_{max} is given by [6, 7]

$$g_{max} = \frac{q^2}{k_{\mathrm{B}}TL^2}\frac{1}{\left\langle\frac{e^{\frac{w(z)}{RT}}}{D(z)}\right\rangle}\frac{1}{\left\langle e^{-\frac{w(z)}{RT}}\right\rangle}, \qquad (2)$$

where q is the quantity of charge an ion carries in coulomb, q= -1.602e^{-19} coulomb here; R is the gas constant 1.987 cal/mol/K; the length L correspond to the region of the channel that represents the rate limiting step for permeation, L=25 Å here. The brackets denote an average over L in the rate-limiting region. We ignore the energy contribution from local molecular interactions and interactions of atomic charges under intrinsic transmembrane potential or external voltage [8], thus w(z) were directly obtained from PMF calculation in kcal/mol.

Diffusion Coefficients. The position-dependent diffusion coefficient D(z) was estimated using the Hummer positional autocorrelation extension of the Woolf−Roux estimator [9, 10]:

$$D(z = \langle z\rangle) = \frac{\mathrm{var}(z)}{\int_0^\infty \frac{C_z(t)\mathrm{d}t}{\mathrm{var}(z)}} = \frac{[\mathrm{var}(z)]^2}{\int_0^\infty C_z(t)\mathrm{d}t}, \qquad (3)$$

where $\langle z\rangle$ is the average of the reaction coordinate z in the biased run; $\mathrm{var}(z) = \langle z^2\rangle - \langle z\rangle^2$ is its variance; $\frac{\int_0^\infty C_z(t)\mathrm{d}t}{\mathrm{var}(z)}$ is the characteristic time of its autocorrelation function (ACF). Position ACF is calculated by

$$C_z(t) = \langle \delta\mathrm{z}(0)\delta\mathrm{z}(t)\rangle = \frac{1}{\mathrm{n_{sample}}}\sum_{\mathrm{i=0}}^{\mathrm{n_{sample}}} \delta\mathrm{z}(i)\delta\mathrm{z}(t+i), \qquad (4)$$

where $\delta z(t) = z(t) - \langle z \rangle$. The ACF_parse.cpp script adapted from the Rowley Lab[11, 12] was used to work with the z-position outputs from US. For each window we calculated ten ACF plots from ten 1-ns periods of a 10-ns length of data, from which we checked if an ACF plot decays to zero. The diffusion profiles along the ion channel are shown in Fig S11, where the rate-limiting region are between -25 and -50 Å corresponding to HBC and G-loop region in the PMFs in Fig 3A. By comparing Fig S11 and Fig 3A, the HBC gate (around -30 Å) that shows small local $D(z)$ value tends to exhibit higher free energy barrier. For example, several US simulations in random PIP_2 system and PIP_2-bound system show small $D(z)$ around 0.5×10^{-5} cm^2/s at -30 Å, while Gβγ-bound systems show larger $D(z)$ above 1×10^{-5} cm^2/s.

Based on Eq. 2, we have the diffusion coefficients $D(z)$ and PMF profile $w(z)$ to calculate the maximum conductance for Gβγ-bound, PIP_2-bound, and random PIP_2 single bilayer systems, which have no membrane potential difference. Double bilayer systems under higher potential difference were also calculated for comparison, although Eq. 2 was reduced for lower membrane potential comparable to cell membrane potential. The estimations from three US simulations are displayed in Table S2 for each system. By taking the maximum g_{max} value for each system, we have 0.04 pS, 0.88 pS, and 123 pS for random PIP_2, PIP_2-bound, and Gβγ-bound single bilayer systems respectively, and 4.7 ± 10^{-14} pS and 47 pS for PIP_2-bound and Gβγ-bound double bilayer systems respectively. In comparison with g from our MD simulations, g_{max} by Eq. 2 underestimate the conductance in PIP_2-bound system, and overestimate conductance in Gβγ-bound single bilayer system, although the g_{max} for Gβγ-bound double bilayer is close to 19.6±10.6 pS from our MD simulations.

Table S2 Maximum conductance (pS) estimation from umbrella sampling.

US No.	random PIP_2	PIP_2-bound	Gβγ-bound	PIP_2-bound (double)	Gβγ-bound (double)
#1	7.3E-05	0.02	123.3	4.4E-14	41.4
#2	2.2E-06	0.14	0.59	4.5E-18	0.14
#3	0.04	0.88	23.9	4.7E-14	47.4

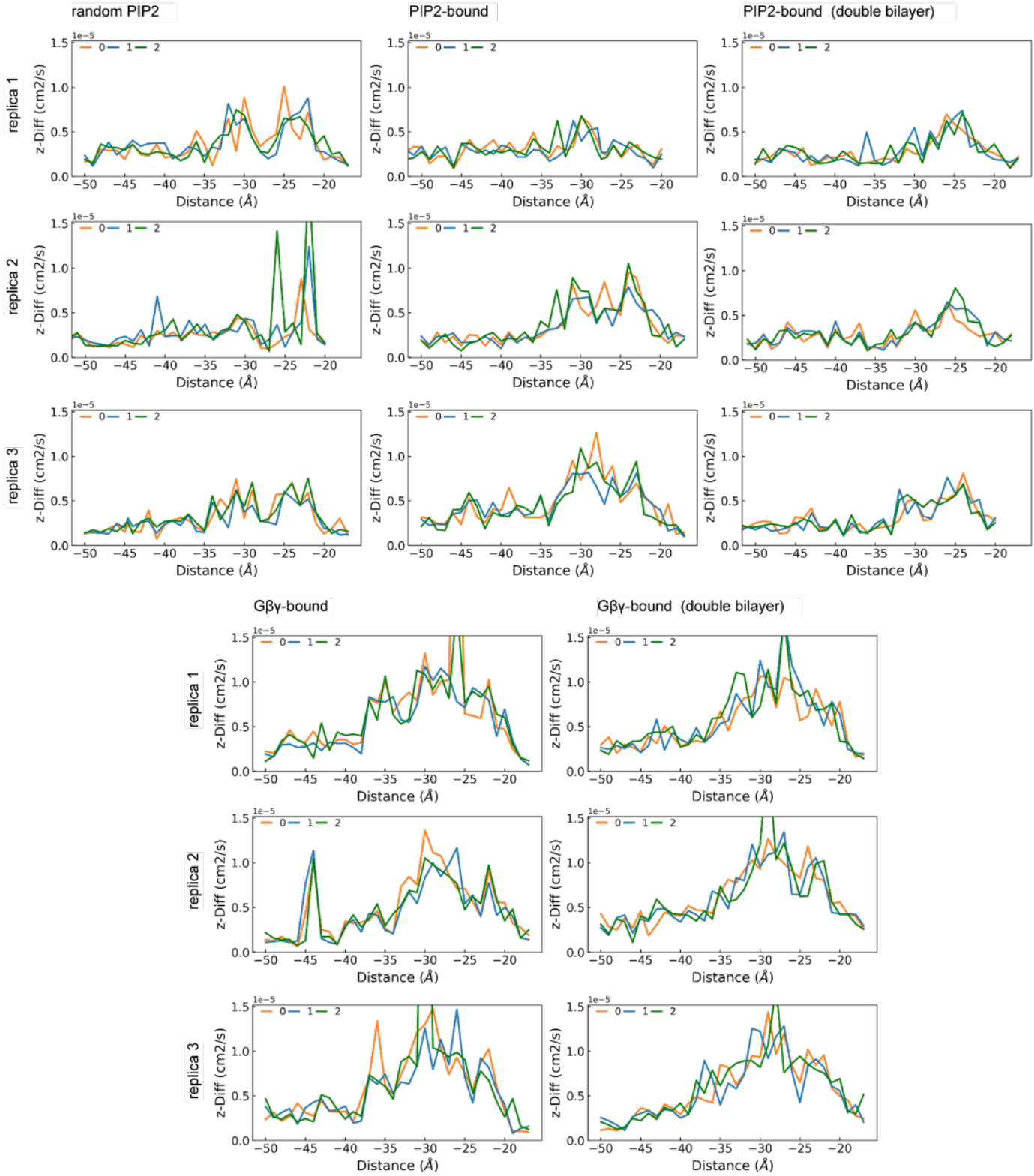

Fig. S11 Diffusion profiles along the channel in random PIP_2, PIP_2-bound, Gβγ-bound single bilayer systems, PIP_2-bound and Gβγ-bound double bilayer systems. Diffusion profiles of three replicas are displayed for each system; three diffusion profiles labeled as 0, 1, 2 in 10-ns interval are displayed in each plot.

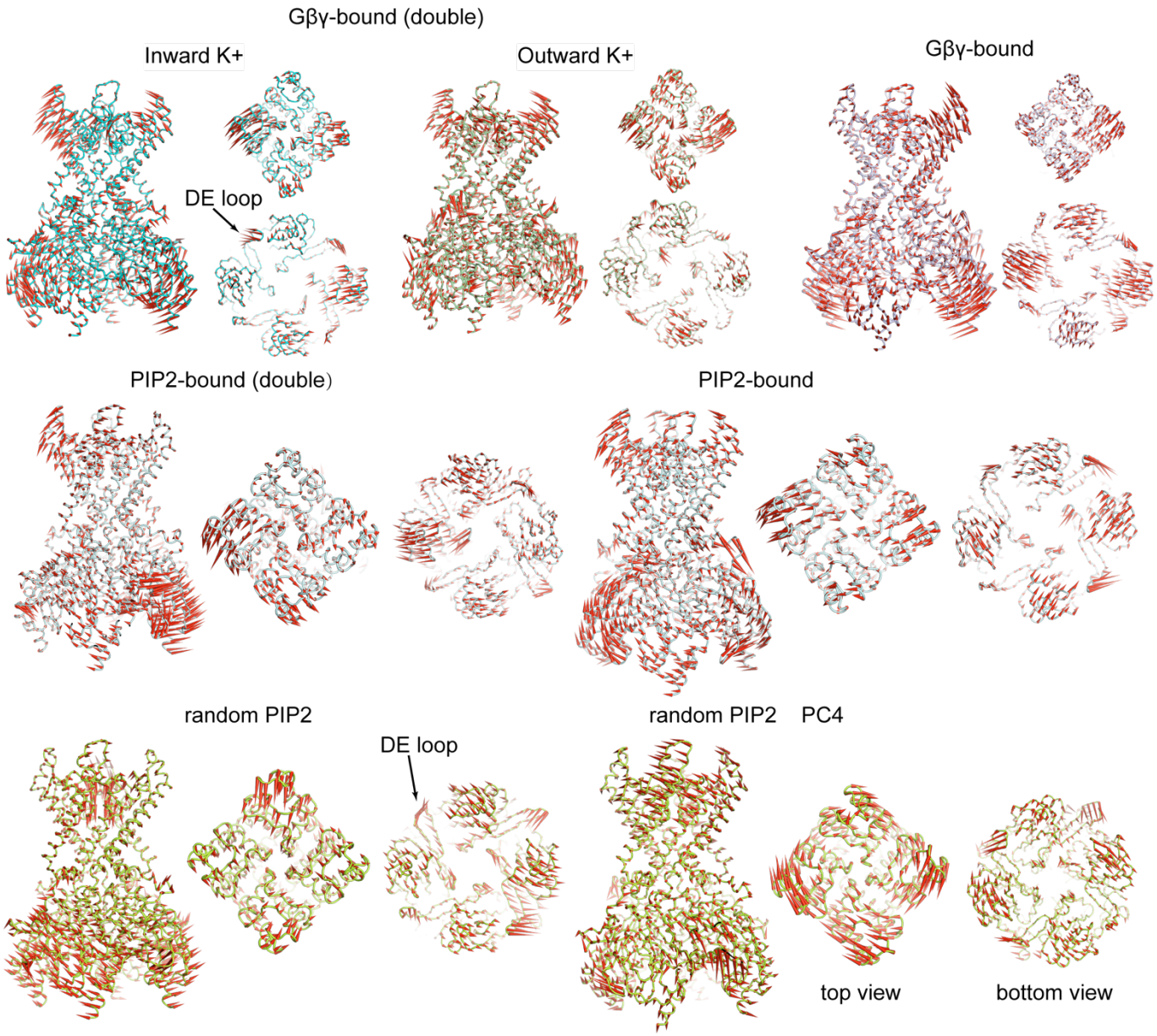

Fig. S12 First principal modes (PC1s). Side view, top view, and bottom view of PC1s of GIRK2 in Gβγ-bound double bilayer systems for inward rectification and outward rectification of K^+, Gβγ-bound single bilayer, PIP_2-bound double bilayer and single bilayer, and random PIP_2 systems. A clockwise rotation from top view of outer helices and bottom view in the CTDs (equivalent to anticlockwise rotation from top view of CTDs) was shown in PC4 of a random PIP_2 replica, but not a dominant mode.

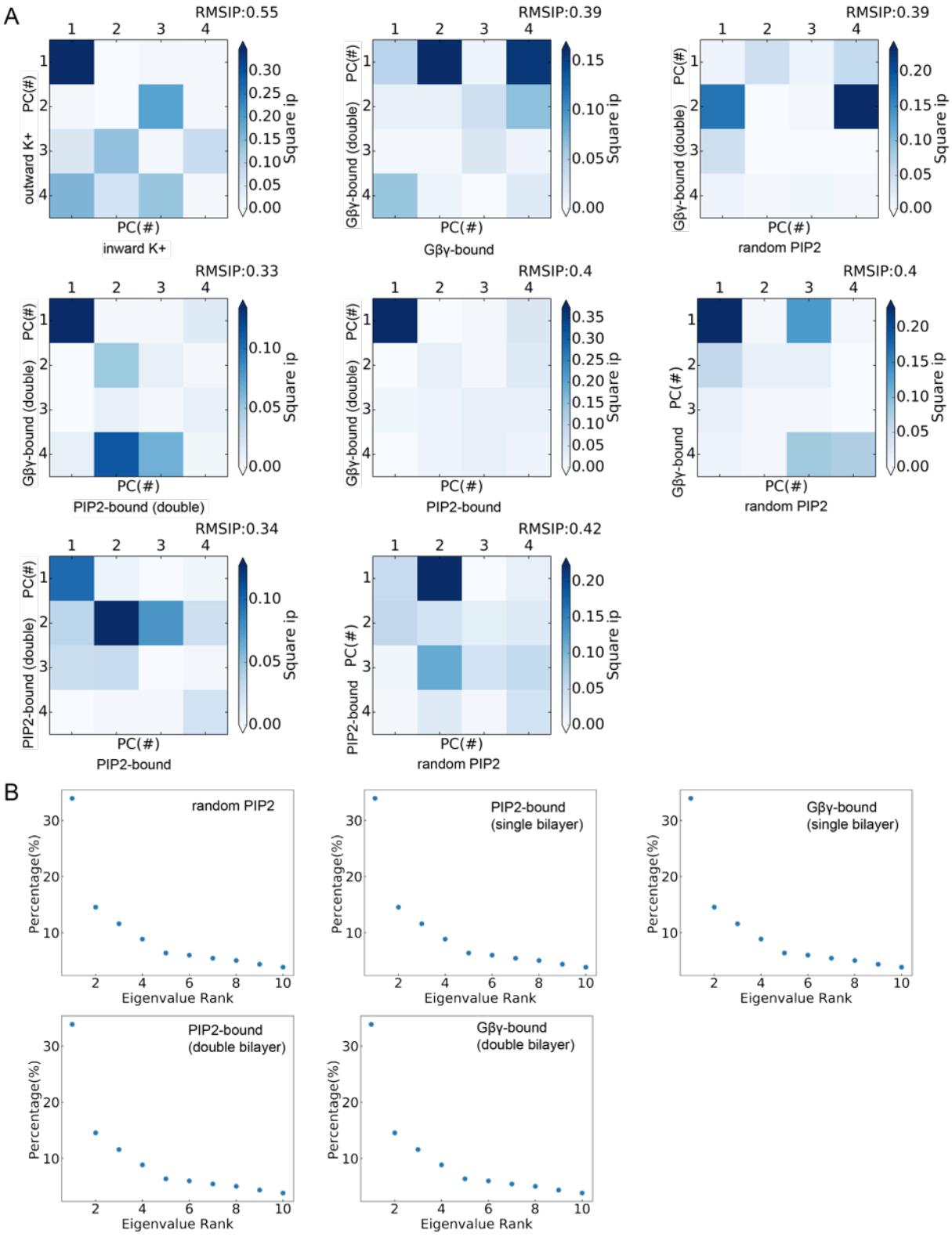

Fig. S13 Root Mean Square Inner Product (RMSIP) and PCA projection percentage. (A) RMSIP between two sets of modes obtained from MD trajectories of random PIP_2, PIP_2-bound, and Gβγ-bound single bilayer systems, PIP_2-bound double bilayer system, and Gβγ-bound double bilayer systems with inward and outward K^+ currents. (B) PCA projection percentage plots for random PIP_2, PIP_2-bound, Gβγ-bound single bilayer systems, PIP_2-bound and Gβγ-bound double bilayer systems.

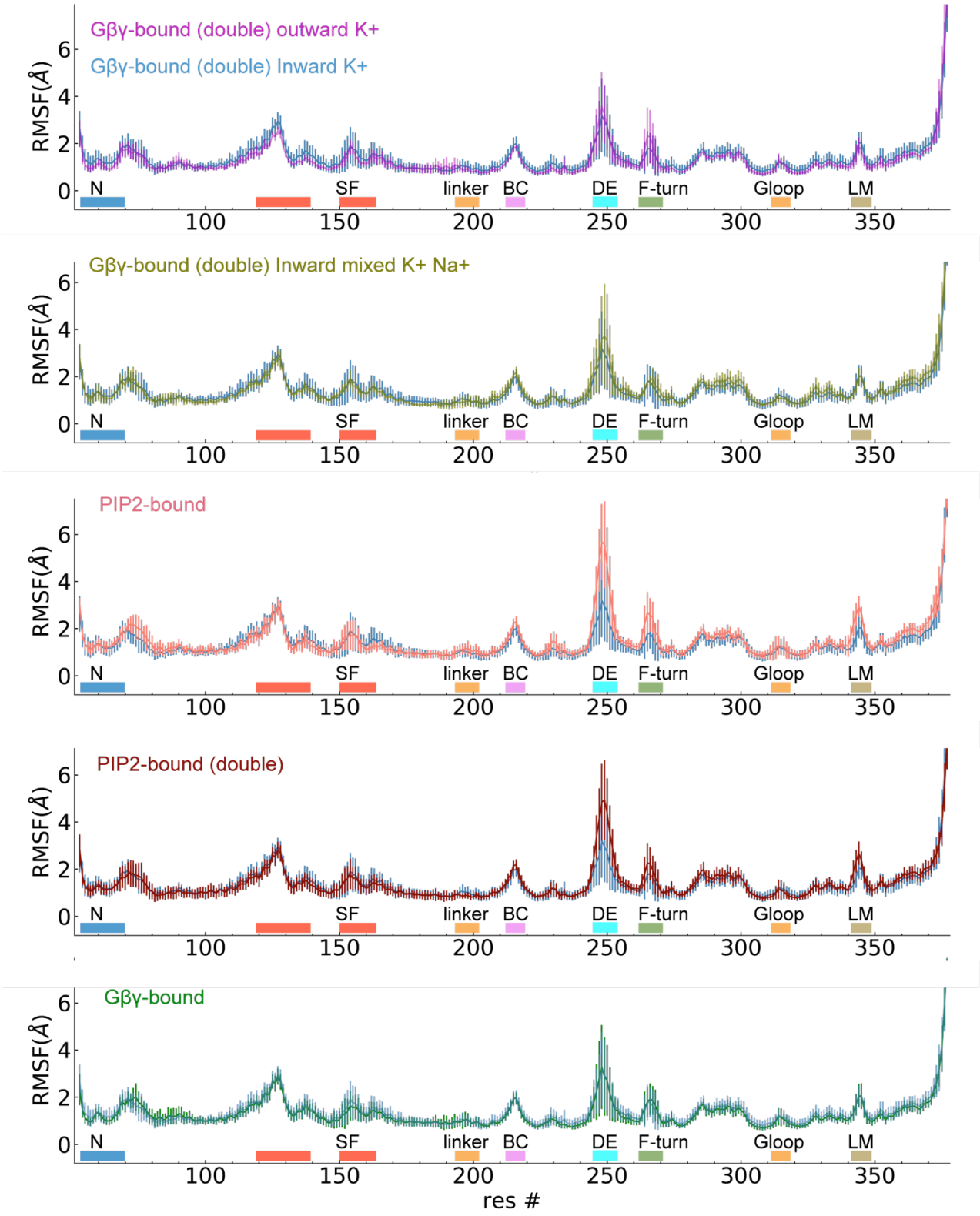

Fig. S14 RMSF per residue of GIRK2 in Gβγ-bound double bilayer system for inward rectification of K^+ (in blue) in comparison with outward rectification of K^+ and inward rectification of mixed K^+ and Na^+, PIP_2-bound, PIP_2-bound double bilayer, Gβγ-bound single bilayer, respectively. RMSF are displayed as averages with standard deviations as error bars.

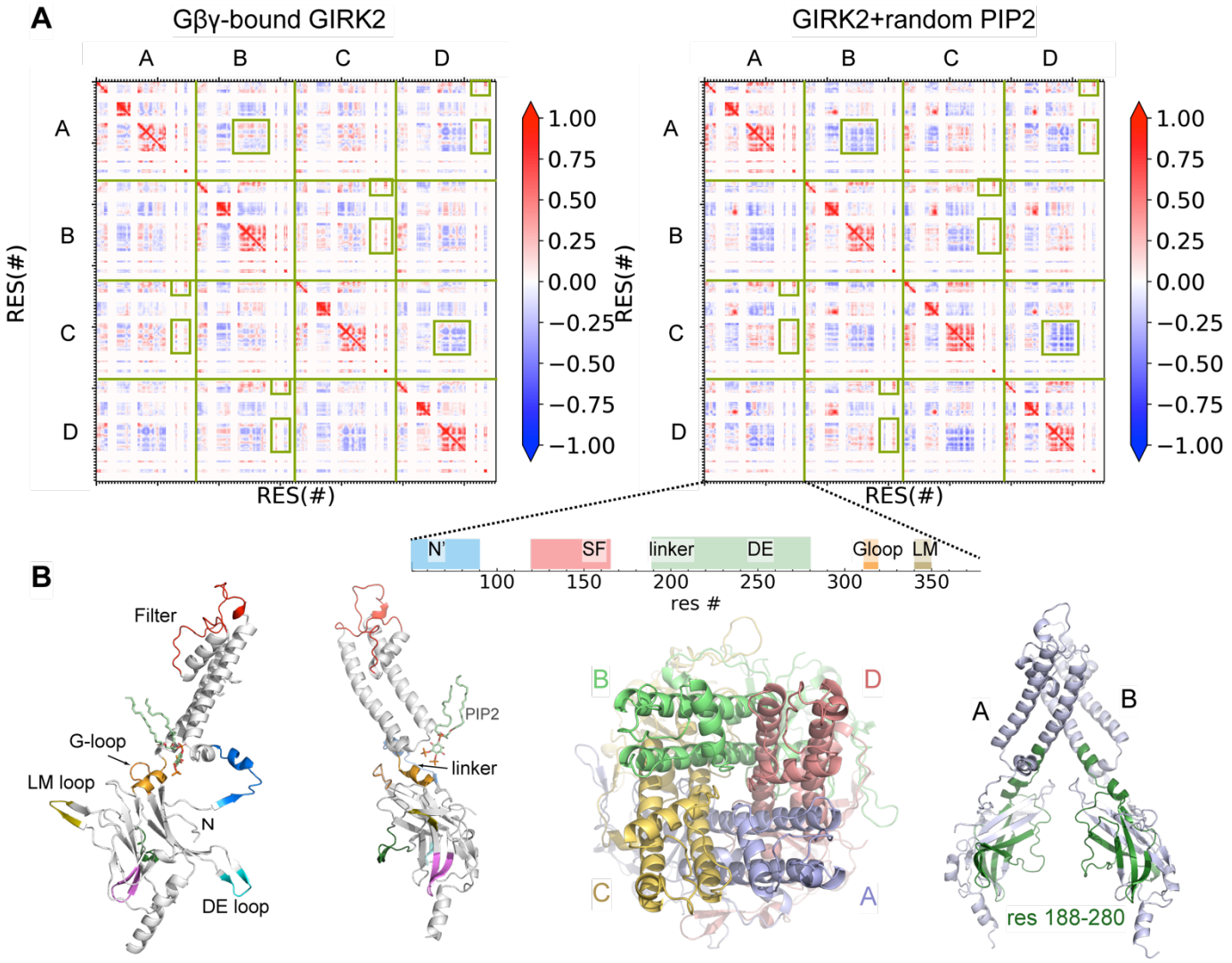

Fig. S15 Dynamic cross correlation maps (DCCMs). (A) DCCMs of random PIP_2 system and Gβγ-bound GIRK2 (+Gβγ) systems with selected shown. (B) Illustration of DCCM sequences positions.

Reference

1. H. Bernsteiner, E. M. Zangerl-Plessl, X. Chen and A. Stary-Weinzinger, *J. Gen. Physiol.*, 2019, **151**, 1231-1246.
2. D. Li, T. Jin, D. Gazgalis, M. Cui and D. E. Logothetis, *J. Biol. Chem.*, 2019, DOI: 10.1074/jbc.RA119.010047.
3. M. R. Whorton and R. MacKinnon, *Cell*, 2011, **147**, 199-208.
4. B. Hille, *Ion Channels of Excitable Membranes* Sinauer Associates Inc., Sunderland, MA U.S.A., 2001.
5. D. G. Levitt, *Annu. Rev. Biophys. Biophys. Chem.*, 1986, **15**, 29-57.
6. B. Roux and M. Karplus, *J. Phys. Chem.*, 1991, **95**, 4856-4868.
7. T. W. Allen, O. S. Andersen and B. Roux, *Biophys. Chem.*, 2006, **124**, 251-267.
8. T. W. Allen, O. S. Andersen and B. Roux, *Proceedings of the National Academy of Sciences*, 2004, **101**, 117.
9. G. Hummer, *New Journal of Physics*, 2005, **7**, 34-34.
10. T. B. Woolf and B. Roux, *JACS*, 1994, **116**, 5916-5926.
11. E. Awoonor-Williams and C. N. Rowley, *Biochimica et Biophysica Acta (BBA) - Biomembranes*, 2016, **1858**, 1672-1687.
12. K. Gaalswyk, E. Awoonor-Williams and C. N. Rowley, *J. Chem. Theory Comput.*, 2016, **12**, 5609-5619.